

## Glass-ceramic joining of Fe22Cr porous alloy to Crofer22APU: interfacial issues and mechanical properties

Fabiana D'Isanto<sup>1\*</sup>, Milena Salvo<sup>1</sup>, Sebastian Molin<sup>2</sup>, Damian Koszelow<sup>2</sup>, Hassan  
Javed<sup>3</sup>, Sufyan Akram<sup>4</sup>, Andreas Chrysanthou<sup>4</sup> and Federico Smeacetto<sup>1</sup>.

<sup>1</sup>Department of Applied Science and Technology, Politecnico di Torino, Corso Duca degli Abruzzi 24,  
10129, Turin, Italy.

<sup>2</sup>Advanced Materials Centre, Faculty of Electronics, Telecommunications and Informatics, Gdańsk  
University of Technology, ul. G. Narutowicza 11/12, 80-233 Gdańsk, Poland.

<sup>3</sup>Sunfire GmbH, Gasanstaltstraße 2, 01237, Dresden, Germany.

<sup>4</sup>School of Physics, Engineering and Computer Science, University of Hertfordshire, College Lane,  
Hatfield, Herts AL10 9AB, UK.

\*Corresponding author.

*E-mail address:* [fabiana.disanto@polito.it](mailto:fabiana.disanto@polito.it) (F. D'Isanto)

Tel +39 011 0904567

### Abstract

This work deals with the joining of porous Fe22Cr ferritic stainless steel to a dense Crofer22APU plate by using a silica-based, Ba-containing glass-ceramic. The chemical and interfacial stability and the mechanical properties of the joints were evaluated before and after thermal ageing at 700°C for 500hrs. The sintering behaviour of the glass was assessed by using heating stage microscopy (HSM) to study the influence of a porous metal substrate on the shrinkage of the joining material. Scanning electron microscopy revealed that there were no defects or cracks at the porous alloy/glass-ceramic interface for both the as-joined samples and the samples after thermal ageing at 700°C for 500 hrs. However, at this exposure temperature, the porous alloy started to form an oxide scale at the interface with the glass-ceramic and the internal surface of

1 the porous alloy. Finally, the evaluation of the mechanical properties by tensile testing  
2  
3 showed that the properties were not affected by thermal ageing at 700°C.  
4  
5  
6  
7

8 **Keywords:** Glass-ceramics; joining; porous alloys; metal-supported SOC  
9

## 10 11 12 13 14 **1. Introduction** 15

16 The porous metallic alloys sector is a major area of interest within the field of high-  
17 temperature engineering materials. The functional role of the porosity can be exploited  
18 in catalytic reactors (thanks to the high surface area for reactions), filters and metal-  
19 supported solid oxide cells (MS-SOCs).  
20  
21  
22  
23  
24

25 Previous studies have evaluated the oxidation resistance of these alloys in the dense  
26 form [1–4] and they have been used for many decades as MS-SOCs [5], but recent  
27 studies on high-temperature corrosion of porous metal alloys [6–9] led to increasing  
28 interest due to important engineering features such as open porosity which allows gas  
29 transport and therefore these materials can be used for gas permeation membranes.  
30  
31  
32  
33  
34  
35  
36  
37

38 Therefore, porous ferritic stainless steels (FSSs) constitute suitable candidate materials  
39 for use as metallic interconnects with high-temperature ceramic fuel cells[9,10] and gas  
40 separation membranes [11–13].  
41  
42  
43  
44

45 Solid oxide cell (SOC) technology has been developed due to its higher efficiency  
46 compared to combustion engines, silent operation and fast charging. Improvements in  
47 materials, cell design and manufacturing processing have led to a very high level of  
48 technical refinement. More recently, due to the tendency of the cell to fail and  
49 assembling issues associated with the use of complex ceramic parts, there has been  
50 interest in alternative MS-SOC which can be exploited in the temperature range of 650-  
51

1 800°C [14] thanks to their low cost, flexibility, robustness and manufacturability  
2  
3 benefits. MS-SOCs allow for a lower cost balance of plant components (BoP) and  
4  
5 higher redox stability.  
6

7  
8 To choose the most suitable material to produce interconnects, it is desirable to  
9  
10 match the coefficient of thermal expansion (CTE) of the metal to that of the  
11  
12 electrolyte[15]. Most manufacturers prefer Fe and Cr-based materials as ferritic  
13  
14 stainless steels (e.g. 430 alloy), which are commonly used for automotive exhaust  
15  
16 manifolds and mufflers thanks to their inexpensive and high-temperature resistance.  
17  
18 This is the reason why FSSs have substituted the more expensive and difficult to  
19  
20 manufacture ceramic interconnects in SOC design [16,17].  
21  
22  
23

24  
25 One of the major challenges in the design of solid oxide cell stacks is the selection  
26  
27 of joining materials for sealing the metallic interconnect. The sealant role is  
28  
29 fundamental to assure high durability and long-term performance. The most common  
30  
31 sealing materials are glass-ceramics due to the simplicity of the sinter-crystallization  
32  
33 process and the possibility to tailor their composition and thermo-mechanical properties.  
34  
35 Moreover, several studies have reported that they can exhibit higher gas tightness than  
36  
37 other typical sealants (i.e. brazing alloys) and superior stability in extreme working  
38  
39 conditions [18–20]. Another advantage of using glass-ceramics is linked to the presence  
40  
41 of a residual glassy phase after the sinter-crystallization process, which can minimize  
42  
43 thermal stresses and provide self-healing properties that are very useful in thermal  
44  
45 cycling conditions [21]. Furthermore, the formation of crystalline phases within the  
46  
47 glass phase improves mechanical properties and drives the choice of the composition in  
48  
49 terms of thermo-mechanical compatibility involving the coefficient of thermal  
50  
51 expansion (CTE) matching with the SOC components[22].

1 The selected sealant inevitably influences the stability and the chemical  
2  
3 compatibility at the interface between the sealant material and the SOC components.  
4  
5 Some studies have shown that undesirable interfacial reactions are possible between Cr-  
6  
7 based stainless steels and glass-ceramic sealants. For example, the BaCrO<sub>4</sub> phase that  
8  
9 has a high CTE (~ 21-23 x 10<sup>-6</sup> K<sup>-1</sup>) can form at the interface between Ba-containing  
10  
11 glass-ceramics and Cr-containing metal interconnects [20,23].  
12  
13  
14

15  
16 Despite this, many research groups have studied and demonstrated the affinity and  
17  
18 the effectiveness of glass-based sealants in solid oxide cells [24–27] and many suitable  
19  
20 BaO-SiO<sub>2</sub>-Al<sub>2</sub>O<sub>3</sub>-based systems have been successfully developed for SOC applications  
21  
22 [25,28], but the current state of the art associated to the joining of porous to bulk alloys  
23  
24 in SOCs by glass-based materials is very limited [29].  
25  
26

27  
28 Previous studies [30] carried out oxidation tests of mixed glass-ceramics with FSS  
29  
30 powders and revealed decreased oxidation rate compared with raw steel powder and  
31  
32 suggested that the resulting oxide scale can enhance the sealant properties.  
33  
34

35  
36 However, very few studies have dealt with the oxidation processes of porous ferritic  
37  
38 stainless steels and there has been no detailed investigation of the joining and  
39  
40 integration issues of these materials. A systematic understanding of how the stainless-  
41  
42 steel porosity and the consequent corrosion reactions affect the interfacial behaviour  
43  
44 with glass-based materials is still lacking.  
45  
46

47  
48 This study describes the joining of porous Fe22Cr alloy to a dense Crofer 22APU  
49  
50 plate with a silica barium-based glass-ceramic. The interfacial behaviour between the  
51  
silica barium-based glass-ceramic and both dense and porous alloy interconnects will be  
discussed with particular focus on the morphological and chemical characterisation at  
the interface before and after thermal ageing at 700°C for 500 h in air. Finally, tensile

1 tests were performed on joined samples, comparing the tensile strength and the fracture  
2 surface between as-joined and aged specimens.  
3  
4  
5  
6  
7

## 8 **2. Materials and methods**

9

10  
11 The Fe22Cr porous alloy substrate (of composition Cr = 22 wt.%; Mn = 0.23 wt.%; Si =  
12 0.08 wt.%; Ni, Cu, Mo <0.03 wt.%, with Fe representing the balance), was produced by  
13  
14 Höganas AB (Höganas, Sweden) and characterised for its resistance against high  
15  
16 temperature oxidation in a study by Koszelow et al [9]. The ~0.4 mm thick porous sheet  
17  
18 was manufactured by tape-casting of a steel particle slurry, followed by drying,  
19  
20 debinding and sintering at 1250°C in a pure H<sub>2</sub> atmosphere for 30 minutes. Dense steel  
21  
22 coupons were cut from a 0.3-mm-thick plate of Crofer22APU (Cr = 23 wt.%, Mn = 0.45  
23  
24 wt.%, La = 0.1 wt.%, Ti = 0.06 wt.%, Si and Al < 0.05 wt.% with Fe representing the  
25  
26 balance) provided by VDM Metals (Verdohl, Germany). Both porous and dense  
27  
28 substrates were cleaned in acetone and ethanol for 10 min each in an ultrasonic bath.  
29  
30  
31 The joining material was a Ba-based glass-ceramic, referred to as GC2 [31]. The  
32  
33 original glass was produced using conventional melting and casting from the following  
34  
35 high-purity grade raw materials: SiO<sub>2</sub> (Sigma Aldrich, 99.5 % purity) with 55 mol%,  
36  
37 B<sub>2</sub>O<sub>3</sub>(precursor H<sub>3</sub>BO<sub>3</sub>, Sigma Aldrich, 99% purity) with 8 mol%, Al<sub>2</sub>O<sub>3</sub> (Alfa Aesar,  
38  
39 99.9 % purity) with 4 mol%, CaO (precursor CaCO<sub>3</sub> Sigma Aldrich, 99 % purity) with 7  
40  
41 mol % and BaO (precursor Ba<sub>2</sub>CO<sub>3</sub> Thermoscientific, 99.8 % purity) with 26 mol%. All  
42  
43 the raw material powders were mixed for 24 hrs and melted in a Pt-Rh crucible in an  
44  
45 electric furnace (LHT418PN2, Nabertherm GmbH, Lilienthal/ Bremen, Germany) in air  
46  
47 at 1500 °C for 1 h (the first 30 minutes a lid covered the crucible). The melt was cast  
48  
49 onto a metal plate and the glass was subsequently ball-milled and sieved (particle  
50  
51

1 size < 38  $\mu\text{m}$ ). The sintering behaviour of the glass powders on the porous substrate, as  
2  
3 well as on  $\text{Al}_2\text{O}_3$  inert substrate was investigated using heating stage microscopy (HSM;  
4 Hesse Heating Microscope, Germany), with a heating rate of  $5^\circ\text{C}/\text{min}$ , from room  
5  
6 temperature up to the melting point identified by the instrument.  
7  
8

9  
10 A small quantity of a slurry paste composed of ethanol (70 wt.%) and glass powder (30  
11 wt.%) was manually deposited with a spatula between the two metal alloys (squared  
12 specimens  $\sim 11\text{ mm} \times \sim 11\text{ mm}$ ) to be joined. Preliminary tests carried out with different  
13 configurations led to the most effective joint with pre-oxidised ( $900^\circ\text{C}$ , 2h as dwelling  
14 time, at a  $5^\circ\text{C}/\text{min}$  as heating/cooling rate) dense Crofer22APU placed on the top. The  
15 joining process was carried out in air at  $950^\circ\text{C}$  for 1h ( $5^\circ\text{C}/\text{min}$  as heating/cooling rate)  
16 in a muffle furnace (L5/13/P330, Nabertherm GmbH, Lilienthal/ Bremen, Germany).  
17

18 During the heat treatment, a stainless-steel weight was placed on top of the sandwich  
19 structure to apply a pressure of around 1.5 kPa. A Computed Tomography (CT) scan  
20 (Fraunhofer IKTS, Hermsdorf, Germany) was used to obtain morphological and  
21 qualitative density information of the joined sample under the following parameters:  
22  
23  $9.25\ \mu\text{m}$  as resolution, 280kV as acceleration voltage and 1s the exposure time for each  
24 projection. The reconstruction of the joint consists of creating a 3D model of the  
25 analysed volume by the CT software.  
26

27 The same heat treatment identified for the joined sample was also used to produce a dry  
28 pressed glass-ceramic pellet, using uniaxial pressure of 12 MPa, to thermo-  
29 mechanically characterise GC2 glass-ceramic. The coefficient of thermal expansion  
30 (CTE) and the dilatometric softening point of as-cast GC2 glass and as-joined glass-  
31 ceramic were measured using a dilatometer (Netzsch, DIL 402 PC) equipped with an  
32  
33  
34  
35  
36  
37  
38  
39  
40  
41  
42  
43  
44  
45  
46  
47  
48  
49  
50  
51

1 alumina sample holder, at a heating rate of 5°C/min, applying a constant compressive  
2  
3 force, between the sample and the piston of 0.25N.  
4

5  
6 Some joined samples were cross-sectioned and prepared for SEM and EDS analyses,  
7  
8 while others were subjected to ageing treatment at 700°C for 500 hrs in a muffle furnace  
9  
10 (Carbolite Gero, Hope Valley, UK). This temperature was chosen based on the results  
11  
12 obtained by Koszelow et al. [9] focused on the corrosion study of the same Fe22Cr  
13  
14 porous alloy up to 900°C. Some joint samples underwent tensile testing before and after  
15  
16 thermal ageing using a method modified from the ASTM C633-01 standard. The tests  
17  
18 were carried out using a Syntech 10/D machine (MTS Systems Corporation, Minnesota,  
19  
20 USA). Each joint was adhered to two loading fixtures (Figure 1) by using Araldite®  
21  
22 2015 epoxy resin and thermally treated at 85°C for 1h to crosslink. The cross-head  
23  
24 speed was set to 0.5 mm/min. The tensile strength was calculated by dividing the  
25  
26 maximum force by the area of the joint which measured 11 mm x 11 mm. A field-  
27  
28 emission scanning electron microscope (FESEM; SupraTM 40, Zeiss, Oberkochen,  
29  
30 Germany) equipped with an energy dispersive X-ray analyser (EDS, Bruker, Germany)  
31  
32 was used to characterise the morphology of the samples, which were previously  
33  
34 polished using SiC papers (grit size 600-4000) and coated with Cr. A benchtop scanning  
35  
36 electron microscope (SEM, JCM-6000 plus, Jeol, Peabody, Massachusetts, USA) was  
37  
38 used to observe the fractured surface of the samples following mechanical testing. X-  
39  
40 ray diffraction (XRD) analysis of the fractured surface of a joined sample after ageing  
41  
42 was conducted using an X'Pert Pro MRD diffractometer, with Cu K $\alpha$  radiation  
43  
44 (PANalytical X'Pert Pro, Philips, Almelo, The Netherlands), and with the aid of X-Pert  
45  
46 HighScore software, while the phases were identified using the JCPDS database  
47  
48  
49  
50  
51

1 provided by PDF-4 ICDD (International Centre for Diffraction Data, Newton Square,  
2  
3 Pennsylvania, the USA).  
4

5  
6 **Figure 1.** Configuration used for the mechanical tensile test.  
7

### 8 9 **3. Results and Discussion**

10  
11 **Figure 2** reports the experimental curves obtained from heating stage microscopy  
12 (HSM) analyses of the as-cast GC2 glass powder pellets on the porous Fe22Cr alloy  
13 (curve 1) and on an inert Al<sub>2</sub>O<sub>3</sub> support (curve 2), where the linear shrinkages % are  
14 (curve 1) and on an inert Al<sub>2</sub>O<sub>3</sub> support (curve 2), where the linear shrinkages % are  
15 plotted against the temperature. The first two characteristic temperatures are the points  
16 at which linear shrinkage of the glass starts ( $T_{fs}$ ) and assumes the maximum value ( $T_{ms}$ ):  
17 they are 705°C and 790°C on the porous alloy, 696°C and 802°C on the Al<sub>2</sub>O<sub>3</sub>  
18 substrate. The temperature at which the first signs of softening are observed (DT) was  
19 identified at 811°C (onto Fe22Cr) and 822°C (onto Al<sub>2</sub>O<sub>3</sub>), while the sphere  
20 temperature (ST) was at 893°C on the porous alloy and 872°C on Al<sub>2</sub>O<sub>3</sub>, where the  
21 height of the sample is equal to the width of the base. The half-sphere temperature (HT),  
22 which is the temperature at which the height of the sample is half the width of the base,  
23 was measured at 1028°C on the Fe22Cr porous alloy and at 1040°C on the inert  
24 substrate. Finally, the flow temperature (FT) was evident at 1079°C and 1076°C; the  
25 latter is the temperature at which the height of the sample drops to below one-third of  
26 the base. A visible plateau between 800 and 1000°C was observed and this represents  
27 the crystallization phenomenon that occurs. A significant expansion of the glass  
28 powder pellet is visible for the GC2 glass onto the Fe22Cr porous alloy, which is  
29 evidently absent on the inert substrate; this is likely due to gaseous species developed at  
30 T higher than 920°C, determined by the oxidation of the porous alloy during the GC2  
31 viscous flow sintering. Based on these observations, the conditions for joining the  
32  
33  
34  
35  
36  
37  
38  
39  
40  
41  
42  
43  
44  
45  
46  
47  
48  
49  
50  
51



1 porous samples to the bulk alloys were determined to be a temperature of 950°C with a  
2  
3 dwelling time of 1h in air. This sinter-crystallization heat treatment led to the formation  
4  
5 of GC2 glass-ceramic with BaSi<sub>2</sub>O<sub>5</sub> as crystalline phase (CTE ~ 12.5 x 10<sup>-6</sup> K<sup>-1</sup>),  
6  
7 obtained by the partial devitrification of the GC2 parent glass [32].  
8  
9

10  
11 **Figure 2.** Heating Stage Microscopy (HSM) curves of the GC2 glass (5°C/min heating rate) on the  
12 Fe22Cr porous alloy (curve 1) and on the inert Al<sub>2</sub>O<sub>3</sub> support (curve 2); characteristic temperatures  
13  
14 of GC2 glass identified with HSM are shown below the figure.  
15  
16  
17

18  
19 In order to evaluate the thermo-mechanical properties of the microstructure obtained  
20  
21 with the above-mentioned joining thermal treatment, dilatometry was used to measure  
22  
23 the coefficient of thermal expansion (CTE) of the GC2 glass-ceramic as well as that of  
24  
25 the parent glass (**Figure 3**). The CTE value of the GC2 as-cast glass is 9.2 x 10<sup>-6</sup> K<sup>-1</sup>  
26  
27 between 200-500°C, while the glass transition temperature (T<sub>g</sub>) and the dilatometric  
28  
29 softening point are 665°C and 688°C respectively (**Figure 3**, curve 1). It can be  
30  
31 observed from the dilatometric analysis of the GC2 glass-ceramic that T<sub>g</sub> is slightly  
32  
33 lower (658°C) with respect to the original glass and within experimental error, while the  
34  
35 softening point is the same. However, there was evidence of an increase in the  
36  
37 coefficient of thermal expansion of the glass-ceramic (10.7 x 10<sup>-6</sup> K<sup>-1</sup>) in comparison  
38  
39 with that of the GC2 glass as suggested by the change in the slope of the curve (**Figure**  
40  
41  
42  
43  
44  
45  
46  
47  
48  
49  
50  
51  
52  
53  
54  
55  
56  
57  
58  
59  
60  
61  
62  
63  
64  
65  
66  
67  
68  
69  
70  
71  
72  
73  
74  
75  
76  
77  
78  
79  
80  
81  
82  
83  
84  
85  
86  
87  
88  
89  
90  
91  
92  
93  
94  
95  
96  
97  
98  
99  
100  
101  
102  
103  
104  
105  
106  
107  
108  
109  
110  
111  
112  
113  
114  
115  
116  
117  
118  
119  
120  
121  
122  
123  
124  
125  
126  
127  
128  
129  
130  
131  
132  
133  
134  
135  
136  
137  
138  
139  
140  
141  
142  
143  
144  
145  
146  
147  
148  
149  
150  
151  
152  
153  
154  
155  
156  
157  
158  
159  
160  
161  
162  
163  
164  
165  
166  
167  
168  
169  
170  
171  
172  
173  
174  
175  
176  
177  
178  
179  
180  
181  
182  
183  
184  
185  
186  
187  
188  
189  
190  
191  
192  
193  
194  
195  
196  
197  
198  
199  
200  
201  
202  
203  
204  
205  
206  
207  
208  
209  
210  
211  
212  
213  
214  
215  
216  
217  
218  
219  
220  
221  
222  
223  
224  
225  
226  
227  
228  
229  
230  
231  
232  
233  
234  
235  
236  
237  
238  
239  
240  
241  
242  
243  
244  
245  
246  
247  
248  
249  
250  
251  
252  
253  
254  
255  
256  
257  
258  
259  
260  
261  
262  
263  
264  
265  
266  
267  
268  
269  
270  
271  
272  
273  
274  
275  
276  
277  
278  
279  
280  
281  
282  
283  
284  
285  
286  
287  
288  
289  
290  
291  
292  
293  
294  
295  
296  
297  
298  
299  
300  
301  
302  
303  
304  
305  
306  
307  
308  
309  
310  
311  
312  
313  
314  
315  
316  
317  
318  
319  
320  
321  
322  
323  
324  
325  
326  
327  
328  
329  
330  
331  
332  
333  
334  
335  
336  
337  
338  
339  
340  
341  
342  
343  
344  
345  
346  
347  
348  
349  
350  
351  
352  
353  
354  
355  
356  
357  
358  
359  
360  
361  
362  
363  
364  
365  
366  
367  
368  
369  
370  
371  
372  
373  
374  
375  
376  
377  
378  
379  
380  
381  
382  
383  
384  
385  
386  
387  
388  
389  
390  
391  
392  
393  
394  
395  
396  
397  
398  
399  
400  
401  
402  
403  
404  
405  
406  
407  
408  
409  
410  
411  
412  
413  
414  
415  
416  
417  
418  
419  
420  
421  
422  
423  
424  
425  
426  
427  
428  
429  
430  
431  
432  
433  
434  
435  
436  
437  
438  
439  
440  
441  
442  
443  
444  
445  
446  
447  
448  
449  
450  
451  
452  
453  
454  
455  
456  
457  
458  
459  
460  
461  
462  
463  
464  
465  
466  
467  
468  
469  
470  
471  
472  
473  
474  
475  
476  
477  
478  
479  
480  
481  
482  
483  
484  
485  
486  
487  
488  
489  
490  
491  
492  
493  
494  
495  
496  
497  
498  
499  
500  
501  
502  
503  
504  
505  
506  
507  
508  
509  
510  
511  
512  
513  
514  
515  
516  
517  
518  
519  
520  
521  
522  
523  
524  
525  
526  
527  
528  
529  
530  
531  
532  
533  
534  
535  
536  
537  
538  
539  
540  
541  
542  
543  
544  
545  
546  
547  
548  
549  
550  
551  
552  
553  
554  
555  
556  
557  
558  
559  
560  
561  
562  
563  
564  
565  
566  
567  
568  
569  
570  
571  
572  
573  
574  
575  
576  
577  
578  
579  
580  
581  
582  
583  
584  
585  
586  
587  
588  
589  
590  
591  
592  
593  
594  
595  
596  
597  
598  
599  
600  
601  
602  
603  
604  
605  
606  
607  
608  
609  
610  
611  
612  
613  
614  
615  
616  
617  
618  
619  
620  
621  
622  
623  
624  
625  
626  
627  
628  
629  
630  
631  
632  
633  
634  
635  
636  
637  
638  
639  
640  
641  
642  
643  
644  
645  
646  
647  
648  
649  
650  
651  
652  
653  
654  
655  
656  
657  
658  
659  
660  
661  
662  
663  
664  
665  
666  
667  
668  
669  
670  
671  
672  
673  
674  
675  
676  
677  
678  
679  
680  
681  
682  
683  
684  
685  
686  
687  
688  
689  
690  
691  
692  
693  
694  
695  
696  
697  
698  
699  
700  
701  
702  
703  
704  
705  
706  
707  
708  
709  
710  
711  
712  
713  
714  
715  
716  
717  
718  
719  
720  
721  
722  
723  
724  
725  
726  
727  
728  
729  
730  
731  
732  
733  
734  
735  
736  
737  
738  
739  
740  
741  
742  
743  
744  
745  
746  
747  
748  
749  
750  
751  
752  
753  
754  
755  
756  
757  
758  
759  
760  
761  
762  
763  
764  
765  
766  
767  
768  
769  
770  
771  
772  
773  
774  
775  
776  
777  
778  
779  
780  
781  
782  
783  
784  
785  
786  
787  
788  
789  
790  
791  
792  
793  
794  
795  
796  
797  
798  
799  
800  
801  
802  
803  
804  
805  
806  
807  
808  
809  
810  
811  
812  
813  
814  
815  
816  
817  
818  
819  
820  
821  
822  
823  
824  
825  
826  
827  
828  
829  
830  
831  
832  
833  
834  
835  
836  
837  
838  
839  
840  
841  
842  
843  
844  
845  
846  
847  
848  
849  
850  
851  
852  
853  
854  
855  
856  
857  
858  
859  
860  
861  
862  
863  
864  
865  
866  
867  
868  
869  
870  
871  
872  
873  
874  
875  
876  
877  
878  
879  
880  
881  
882  
883  
884  
885  
886  
887  
888  
889  
890  
891  
892  
893  
894  
895  
896  
897  
898  
899  
900  
901  
902  
903  
904  
905  
906  
907  
908  
909  
910  
911  
912  
913  
914  
915  
916  
917  
918  
919  
920  
921  
922  
923  
924  
925  
926  
927  
928  
929  
930  
931  
932  
933  
934  
935  
936  
937  
938  
939  
940  
941  
942  
943  
944  
945  
946  
947  
948  
949  
950  
951  
952  
953  
954  
955  
956  
957  
958  
959  
960  
961  
962  
963  
964  
965  
966  
967  
968  
969  
970  
971  
972  
973  
974  
975  
976  
977  
978  
979  
980  
981  
982  
983  
984  
985  
986  
987  
988  
989  
990  
991  
992  
993  
994  
995  
996  
997  
998  
999  
1000

**Figure 3.** Dilatometric curves of the GC2 as-cast glass (curve 1) and GC2 glass-ceramic obtained after sinter-crystallization at 950°C for 1h (curve 2); 5°C/min heating rate.

1  
2  
3 The sandwiched samples were processed, using the procedure described in the  
4  
5 experimental section.  
6

7  
8 As observed in [Figure 4 a](#), the SEM image of the cross-section of the joined sample  
9  
10 showed excellent adhesion of the GC2 glass-ceramic with both the porous and dense  
11  
12 metal alloys. No cracks or delamination are visible at the glass-ceramic/substrates  
13  
14 interface resulting in a continuous joint along the entire length of the interface.  
15  
16 Furthermore, there was no evidence of any reactions taking place by the interaction  
17  
18 between the Crofer22APU/porous alloy and the glass ([Figure 4 b,c](#)) ; an average joint  
19  
20 thickness of 520  $\mu\text{m}$  was obtained using a pressure of 1.5 kPa. The presence of a few  
21  
22 closed pores, homogeneously distributed in the glass-ceramic, could probably be due to  
23  
24 the manual slurry method used to produce the joined specimens. On the other side, the  
25  
26 larger voids observed only at the Fe22Cr porous alloy/GC2 glass-ceramic interface is  
27  
28 probably due to gaseous species released from the porous substrate during sintering  
29  
30 which occurred by viscous flow. Further SEM investigation carried out on a  
31  
32 Crofer22APU/GC2 glass-ceramic/Crofer22APU joint (not reported here), showed the  
33  
34 absence of these such big voids at both dense alloy/glass-ceramic interfaces, thus  
35  
36 confirming that the bigger porosity is due only to the presence of the Fe22Cr porous  
37  
38 alloy.  
39

40  
41  
42 [Figure 4](#). SEM images of the cross-section of (a) Crofer22APU/GC2 glass-ceramic/Fe22Cr porous  
43  
44 alloy, (b) Crofer22APU/GC2 glass-ceramic interface (back-scattered) and (c) GC2 glass-  
45  
46 ceramic/Fe22Cr porous alloy interface (back-scattered) obtained after sinter-crystallization at 950°C  
47  
48 for 1h.  
49  
50  
51

1 Most of the porosity was concentrated at the porous alloy/GC2 glass-ceramic interface  
2  
3 as evidenced by SEM as well as computed tomography (CT) that was carried out on a  
4  
5 joined sandwich-like specimen (Figure 5). In Figure 5a, a reconstructed 3D model of  
6  
7 the sample is shown, while in the other images (Figure 5 b-d), 3 cross-sections are  
8  
9 represented at a different distance from the porous alloy surface; these scans were taken  
10  
11 close to the Fe22Cr/GC2 glass-ceramic interface (Figure 5b), in the middle of the  
12  
13 joining area (Figure 5c) and finally further from the interface with the porous alloy. It is  
14  
15 evident that most voids are located at the Fe22Cr/GC2 glass-ceramic interface, while in  
16  
17 the other sections very few pores are shown.  
18  
19  
20  
21  
22

23 **Figure 5.** CT-scan of a Crofer22APU/GC2 glass-ceramic/Fe22Cr porous alloy joined sample  
24 thermally treated at 950°C for 1 h. (a) 3D-model; sectioning plane (b) close to the porous alloy, (c)  
25 in the middle of the glass-ceramic, (d) close to Crofer22APU. The big pore on the right could be due  
26 to the manual slurry method used to produce the joined specimen.  
27  
28  
29  
30  
31

32  
33 More details concerning the Fe22Cr porous alloy/GC2 glass-ceramic interface are  
34 shown in FE-SEM images on a cross-sectioned joined sample in Figure 6. Close  
35 inspection at the interface shows that, despite the presence of pores that are concentrated  
36 in the lower part of the joining area, no cracks are located both in the joining area and at  
37 the interface. Strong adhesion between the GC2 glass-ceramic and the porous substrate  
38 can be observed (Figure 6a). The distribution of the crystalline phases produces a dense  
39 network of needle-like interlocked crystallites embedded in the residual glassy phase.  
40 EDS analysis in Figure 6d (spectrum 1) revealed the presence of Ba, Si and O,  
41 indicating the crystallization of a BaSi<sub>2</sub>O<sub>5</sub> crystalline phase, homogeneously dispersed  
42 within the darker glassy matrix which reasonably shows a higher level of Al and Ca and  
43 a lower content of Ba and Si (spectrum 2); this hypothesis was supported by XRD  
44  
45  
46  
47  
48  
49  
50  
51

1 diffraction pattern of GC2 glass-ceramic after joining heat treatment at 950°C, 1h in air,  
2  
3 as reported by Smeacetto et al. [32]. As shown in Figure 6c and the corresponding EDS  
4  
5 in Figure 6d (spectrum 3), the glass infiltrates the porous alloy very well during the  
6  
7 sinter-crystallization treatment; infiltration distance levels of up to 50 μm from the GC2  
8  
9 glass-ceramic/Fe22Cr porous alloy interface are evident.  
10  
11  
12

13  
14 **Figure 6.** Cross-section FE-SEM images at lower (a) and higher (b) magnification of the Fe22Cr  
15 porous alloy/GC2 glass-ceramic interface after sinter-crystallization at 950°C for 1h; (c) infiltration  
16 of the glass-ceramic in the porous alloy of the joined sample; (d) EDS analyses of the GC2 glass-  
17 ceramic in the joining area.  
18  
19  
20  
21

22  
23 Tensile testing was used to evaluate the mechanical properties of the joined  
24 samples. The tests carried out on as-joined Crofer22APU/GC2 glass-ceramic/Fe22Cr  
25 porous alloy samples showed an average tensile strength of  $7.4 \pm 0.5$  MPa (identified  
26 with  $\sigma_m$  in Figure 7). This value is slightly higher than the tensile strength of the  
27 majority of glass-ceramic sealants reported in the literature (3.8-6.3 MPa) and used for  
28 joining Crofer22APU and Crofer22H [33].  
29  
30  
31  
32  
33  
34  
35  
36  
37

38  
39 **Figure 7.** Macrographs of as-joined and aged Crofer22APU/GC2glass-ceramic/ Fe22Cr samples  
40 after tensile testing.  
41

42  
43 Macrographs of the fracture surface of 3 as-joined specimens are shown in Figure 7.  
44 While most of the fractured area of the Fe22Cr porous substrate in Figure 7 seems to  
45 show exposed metal alloy, however, EDS analyses (not reported here) revealed many  
46 parts of the surface covered by the GC2 glass-ceramic; in some areas, large sections (in  
47 white) of the GC2 glass-ceramic suggest the presence of cohesive failure, while small  
48 white specks show evidence of fractured glass-ceramic that had impregnated the pores  
49 of the Fe22Cr substrate. Inspection of the opposite part shows small fractured black  
50  
51

1 specks of Fe22Cr embedded in the GC2 glass-ceramic. These observations suggest that  
2  
3 the impregnation of the glass-ceramic into the Fe22Cr porous alloy enhances the  
4  
5 interfacial strength. Indeed, part of the failure seems to be occurring in the porous  
6  
7 Fe22Cr just beyond the area of GC2 impregnation due to stress concentration in the  
8  
9 porous alloy (due to the absence of GC2 glass-ceramic). Overall there is mixed  
10  
11 adhesive/cohesive failure, where the adhesive failure is mainly localised at the  
12  
13 porous/GC2 interface. [Figure 8a](#) shows a magnified fracture surface of the glass-  
14  
15 ceramic on the Crofer22APU side after mechanical testing; the bright phase well visible  
16  
17 in the back-scattered SEM image identified by the EDS analysis as BaCrO<sub>4</sub>, was mainly  
18  
19 located on the edges of the joined area and was present on both the porous and the dense  
20  
21 metal alloy.  
22  
23  
24  
25  
26

27  
28 [Figure 8](#). SEM images of top views of fracture surface of an as-joined (a) and an aged (b)  
29  
30 Crofer22APU/GC2glass-ceramic/ Fe22Cr porous alloy sample after mechanical testing  
31  
32 (Crofer22APU side); EDS analyses carried out on the fracture surfaces in the joining area.  
33  
34  
35

36  
37 [Figure 9](#) shows a cross-section of a joined sample after ageing at 700°C for 500 hrs.  
38  
39 There was no evidence of cracks following ageing, thus implying that detrimental  
40  
41 thermal stresses did not occur. In addition, the microstructure of the GC2 glass-ceramic  
42  
43 did not seem to be affected by the heat treatment ([Figure 9a](#)). However, [Figure 9b](#)  
44  
45 shows evidence of the formation of an oxidation scale on the pores surface; oxidation  
46  
47 was also apparent at the GC2 glass-ceramic/porous alloy interface ([Figure 9c](#)). Due to  
48  
49 the large surface/volume ratio of the porous samples, there is a risk that oxide formation  
50  
51 (typically Cr<sub>2</sub>O<sub>3</sub> [34]) can potentially lead to depletion of Cr within the porous alloy. In  
a previously cited work [9], the surface of the same porous alloy, which was exposed to  
a temperature of 700°C for 100hrs, did not show any significant microstructural changes

1 in comparison to alloy samples that had not been aged. The weight gain at 700°C after  
2  
3  
4 100 hrs was reported to be around 1%. However, a sample that had been exposed to  
5  
6 750°C for the same time, experienced a weight gain of ~2.5 % and was characterised by  
7  
8 changes at the surface; a small amount of oxide had clearly formed at the surface which  
9  
10 exhibited signs of greater roughness which may have resulted by the fact that the  
11  
12 surface of the porous alloy was slightly rough. From [Figure 9d](#) the formation of a  
13  
14 darker layer covering the Fe22Cr porous alloy following ageing is apparent. Based on  
15  
16 the results of the EDS analysis the scale seems to be composed of a mixed Fe and Cr-  
17  
18 based oxide and, since the latter is visible also further from the glass-ceramic/Fe22Cr  
19  
20 porous alloy interface, it could be due to a longer ageing heat treatment (700°C for  
21  
22 500hrs).

23  
24  
25  
26  
27 [Figure 9](#). FE-SEM images of a cross-section after ageing at 700°C for 500hrs: (a,c) Fe22Cr porous  
28  
29 alloy/GC2 glass-ceramic interface and (b) Fe22Cr porous alloy; (d) higher magnification of Fe22Cr  
30  
31 porous alloy and EDS analysis carried out on the porosity edge of the porous alloy.  
32  
33

34  
35  
36 The results of mechanical testing for the thermally-aged samples exhibited an  
37  
38 average tensile strength of  $7.7 \pm 2.9$  MPa, a value that was similar to the as-joined  
39  
40 samples. Inspection of the macrographs in [Figure 7](#) shows that the samples suffered a  
41  
42 completely or mainly adhesive failure. [Figure 8b](#) shows a higher magnification of the  
43  
44 fracture surface of the Crofer22APU after ageing at 700°C for 500 hrs following  
45  
46 mechanical testing. The EDS analysis showed high atomic% of Ba and Cr and therefore  
47  
48 the presence of barium chromate can be hypothesized also after ageing .  
49  
50  
51

XRD analysis that was carried out on the Crofer22APU side (on the porous side, the remaining glass-ceramic layer was not enough) after ageing and mechanical testing, is shown in [Figure 10](#). The main peaks matched with those of the orthorhombic barium



1 silicate (Sanbornite with chemical formula  $\text{BaSi}_2\text{O}_5$ , PDF card n. 01-071-1441), which  
2  
3 was the main phase present after ageing. Prior to the ageing treatment, the only phase  
4  
5 that was present was  $\text{BaSi}_2\text{O}_5$  as previously reported for the as joined glass-ceramic  
6  
7 system before ageing heat treatment [32]. However, following ageing, new phases  
8  
9 emerged like those reported in previous studies with similar glasses [25], where the  
10  
11 formation of additional Ba-Ca-silicate phases that were not homogeneously distributed  
12  
13 within the microstructure was observed. In the present work a secondary phase  
14  
15 identified as the barium calcium boron silicate (named Itsiite[35], crystal system:  
16  
17 tetragonal; space group: I-42m)  $\text{Ba}_2\text{CaSi}_4\text{B}_2\text{O}_{14}$ , with PDF card n. 04-021-1159 was  
18  
19 found. In addition, some low-intensity peaks were identified as the  $\text{BaCrO}_4$  phase,  
20  
21 confirming the EDS analyses carried out at the same fracture surface. Finally, the three  
22  
23 peaks at about  $2\theta=22.8^\circ$ ,  $2\theta = 30.2^\circ$  and  $2\theta=34.5^\circ$  could likely be attributed to  
24  
25  $\text{BaAl}_2\text{Si}_2\text{O}_8$  (ref. code 00-012-0725). In the present work, the glass-ceramic joining  
26  
27 material was subjected to a thermal ageing temperature that was  $40^\circ\text{C}$  higher than the  
28  
29 GC2 glass-ceramic  $T_g$  value. These findings, while preliminary, suggest that this  
30  
31 system is prone to further devitrification at temperatures slightly above the  $T_g$ . Despite  
32  
33 this, the mechanical behaviour of the joints is not affected by this microstructural  
34  
35 rearrangement. Further research should be undertaken to investigate the  
36  
37 thermomechanical behaviour at temperatures higher than  $700^\circ\text{C}$ .  
38  
39  
40  
41  
42  
43  
44  
45  
46  
47  
48  
49  
50  
51

Figure 10. XRD pattern of the fracture surface (Crofer22APU side) of a Fe22Cr/GC2 glass-ceramic/Crofer22APU joined sample after ageing at  $700^\circ\text{C}$  for 500 hrs.

#### 4. Conclusions

1 The possibility of using porous metal alloys provides interesting engineering  
2  
3 features thanks to their functional porosity, which make these candidate materials for  
4  
5 metal-supported solid oxide cells. The development of a dense to a porous joint can  
6  
7 play a key role in the manufacture of reliable, efficient and durable metal-supported  
8  
9 SOCs. The novelty of this study concerns the joining of porous stainless steel to a  
10  
11 dense one with a glass-ceramic obtained from sinter-crystallization of a glass sealant.  
12  
13 Different aspects concerning the interfacial issues and mechanical properties were  
14  
15 discussed, evaluating an optimal adhesion and mechanical stability in  
16  
17 Crofer22APU/GC2 glass-ceramic/ Fe22Cr porous alloy joints, before and after thermal  
18  
19 ageing carried out at 700°C for 500hrs. The morphological analysis found no defects or  
20  
21 cracks at the porous alloy/glass-ceramic interface, neither in the as-joined samples nor  
22  
23 in samples after ageing at 700°C for 500 hrs. However, at this temperature, the porous  
24  
25 alloy started to experience the formation of an oxidation scale at the interface between  
26  
27 the Fe22Cr porous alloy and the GC2 glass-ceramic, as well as around the wall of the  
28  
29 pores of the porous alloy. The mechanical strength of the joined samples was not  
30  
31 affected by thermal ageing (7.4 MPa±0.5 before and 7.7 MPa ±2.9 after ageing).  
32  
33  
34  
35  
36  
37  
38

39 The current study provides the first assessment concerning the joining of a porous  
40  
41 to a dense alloy using glass-ceramics and makes the groundwork for future research into  
42  
43 MS-SOC development.  
44  
45  
46  
47  
48  
49

### 50 **Acknowledgments**

51 DK and SM acknowledge the support of National Science Centre Poland (NCN)  
Sonata Bis 8 project number 2018/30/E/ST8/00821 “High-temperature corrosion studies



1 and development of oxidation lifetime model of alloy powders and sintered porous alloys:  
2  
3 effects of composition and microstructure”.  
4  
5  
6  
7  
8

### 9 **Declaration of competing interest**

10  
11 The authors declare that they have no known competing financial interests or personal  
12 relationships that could have appeared to influence the work reported in this paper.  
13  
14  
15  
16  
17

### 18 **References**

- 19  
20  
21 [1] J.E. Hammer, S.J. Laney, R.W. Jackson, K. Coyne, F.S. Pettit, G.H. Meier, The  
22 oxidation of ferritic stainless steels in simulated solid-oxide fuel-cell atmospheres,  
23 Oxid. Met. 67 (2007) 1–38. <https://doi.org/10.1007/s11085-006-9041-y>.  
24  
25  
26  
27  
28 [2] N.J. Magdefrau, L. Chen, E.Y. Sun, M. Aindow, Effects of alloy heat treatment on  
29 oxidation kinetics and scale morphology for crofer 22 APU, J. Power Sources. 241  
30 (2013) 756–767. <https://doi.org/10.1016/j.jpowsour.2013.03.181>.  
31  
32  
33  
34  
35 [3] P. Alnegren, M. Sattari, J. Froitzheim, J.E. Svensson, Degradation of ferritic  
36 stainless steels under conditions used for solid oxide fuel cells and electrolyzers at  
37 varying oxygen pressures, Corros. Sci. 110 (2016) 200–212.  
38 <https://doi.org/10.1016/j.corsci.2016.04.030>.  
39  
40  
41  
42  
43 [4] B. Timurkutluk, S. Toros, S. Onbilgin, H.G. Korkmaz, Determination of  
44 formability characteristics of Crofer 22 APU sheets as interconnector for solid  
45 oxide fuel cells, Int. J. Hydrogen Energy. 43 (2018) 14638–14647.  
46 <https://doi.org/10.1016/j.ijhydene.2018.04.243>.  
47  
48  
49  
50  
51 [5] S. Fontana, R. Amendola, S. Chevalier, P. Piccardo, G. Caboche, M. Viviani, R.  
Molins, M. Sennour, Metallic interconnects for SOFC: Characterisation of

- 1 corrosion resistance and conductivity evaluation at operating temperature of  
2 differently coated alloys, *J. Power Sources*. 171 (2007) 652–662.  
3  
4  
5  
6 <https://doi.org/10.1016/j.jpowsour.2007.06.255>.  
7
- [6] D.N. Boccaccini, H.L. Frandsen, B.R. Sudireddy, P. Blennow, H. Persson, K.  
8 Kwok, P. Vang Hendriksen, Creep behaviour of porous metal supports for solid  
9 oxide fuel cells, *Int. J. Hydrogen Energy*. 39 (2014) 21569–21580.  
10  
11 <https://doi.org/10.1016/j.ijhydene.2014.07.138>.  
12  
13
- [7] M. Stange, C. Denonville, Y. Larring, A. Brevet, A. Montani, O. Sicardy, J.  
14 Mougín, P.O. Larsson, Improvement of corrosion properties of porous alloy  
15 supports for solid oxide fuel cells, *Int. J. Hydrogen Energy*. 42 (2017) 12485–  
16 12495. <https://doi.org/10.1016/j.ijhydene.2017.03.170>.  
17  
18
- [8] E. Stefan, C. Denonville, Y. Larring, M. Stange, R. Haugrud, Oxidation study of  
19 porous metal substrates for metal supported proton ceramic electrolyzer cells,  
20  
21 *Corros. Sci.* 164 (2020) 108335. <https://doi.org/10.1016/j.corsci.2019.108335>.  
22  
23  
24
- [9] D. Koszelow, M. Makowska, F. Marone, J. Karczewski, P. Jasiński, S. Molin, High  
25 temperature corrosion evaluation and lifetime prediction of porous Fe22Cr  
26 stainless steel in air in temperature range 700–900 °C, *Corros. Sci.* 189 (2021).  
27  
28 <https://doi.org/10.1016/j.corsci.2021.109589>.  
29  
30  
31  
32
- [10] V. Venkatachalam, S. Molin, M. Chen, I. Smirnov, P.O. Larsson, P. V.  
33 Hendriksen, N. Bonanos, Optimization of ferritic steel porous supports for protonic  
34 fuel cells working at 600°C, *Mater. Sci. Technol. Conf. Exhib. 2014, MS T 2014*.  
35  
36 2 (2014) 1231–1239.  
37  
38
- [11] Y. Xing, S. Baumann, D. Sebold, M. Rüttinger, A. Venskutonis, W.A.  
39 Meulenberg, D. Stöver, Chemical compatibility investigation of thin-film oxygen  
40  
41  
42  
43  
44  
45  
46  
47  
48  
49  
50  
51

- 1 transport membranes on metallic substrates, *J. Am. Ceram. Soc.* 94 (2011) 861–  
2 866. <https://doi.org/10.1111/j.1551-2916.2010.04171.x>.
- 3  
4  
5  
6 [12] J.A. Calles, R. Sanz, D. Alique, Influence of the type of siliceous material used as  
7 intermediate layer in the preparation of hydrogen selective palladium composite  
8 membranes over a porous stainless steel support, *Int. J. Hydrogen Energy.* 37  
9 (2012) 6030–6042. <https://doi.org/10.1016/j.ijhydene.2011.12.164>.
- 10  
11  
12  
13 [13] J.A. Glasscock, L. Mikkelsen, Å.H. Persson, G. Pećanac, J. Malzbender, P.  
14 Blennow, F. Bozza, P. V. Hendriksen, Porous Fe<sub>21</sub>Cr<sub>7</sub>Al<sub>1</sub>Mo<sub>0.5</sub>Y metal supports  
15 for oxygen transport membranes: Thermo-mechanical properties, sintering and  
16 corrosion behaviour, *Solid State Ionics.* 242 (2013) 33–44.  
17 <https://doi.org/10.1016/j.ssi.2013.04.006>.
- 18  
19  
20  
21 [14] S. Linderoth, Solid oxide cell R&D at Risø National Laboratory-and its transfer to  
22 technology, *J. Electroceramics.* 22 (2009) 61–66. [https://doi.org/10.1007/s10832-](https://doi.org/10.1007/s10832-008-9458-6)  
23 [008-9458-6](https://doi.org/10.1007/s10832-008-9458-6).
- 24  
25  
26 [15] M.C. Tucker, Progress in metal-supported solid oxide fuel cells: A review, *J.*  
27 *Power Sources.* 195 (2010) 4570–4582.  
28 <https://doi.org/10.1016/j.jpowsour.2010.02.035>.
- 29  
30  
31 [16] M.C. Tucker, G.Y. Lau, C.P. Jacobson, L.C. DeJonghe, S.J. Visco, Stability and  
32 robustness of metal-supported SOFCs, *J. Power Sources.* 175 (2008) 447–451.  
33 <https://doi.org/10.1016/j.jpowsour.2007.09.032>.
- 34  
35  
36 [17] M.C. Tucker, Durability of symmetric-structured metal-supported solid oxide fuel  
37 cells, *J. Power Sources.* 369 (2017) 6–12.  
38 <https://doi.org/10.1016/j.jpowsour.2017.09.075>.
- 39  
40  
41 [18] J.W. Fergus, Sealants for solid oxide fuel cells, *J. Power Sources.* 147 (2005) 46–

- 1 57. <https://doi.org/10.1016/j.jpowsour.2005.05.002>.
- 2
- 3 [19] M.K. Mahapatra, K. Lu, Seal glass for solid oxide fuel cells, *J. Power Sources*. 195
- 4 (2010) 7129–7139. <https://doi.org/10.1016/j.jpowsour.2010.06.003>.
- 5
- 6 [20] N. Mahato, A. Banerjee, A. Gupta, S. Omar, K. Balani, Progress in material
- 7 selection for solid oxide fuel cell technology: A review, *Prog. Mater. Sci.* 72 (2015)
- 8 141–337. <https://doi.org/10.1016/j.pmatsci.2015.01.001>.
- 9
- 10 [21] R.N. Singh, Sealing Technology for Solid Oxide Fuel Cells (SOFC), *Int. J. Appl.*
- 11 *Ceram. Technol.* 4 (2007) 134–144. [https://doi.org/10.1111/j.1744-](https://doi.org/10.1111/j.1744-7402.2007.02128.x)
- 12 [7402.2007.02128.x](https://doi.org/10.1111/j.1744-7402.2007.02128.x).
- 13
- 14 [22] F. Smeacetto, A. De Miranda, A. Chrysanthou, E. Bernardo, M. Secco, M. Bindi,
- 15 M. Salvo, A.G. Sabato, M. Ferraris, Novel glass-ceramic composition as sealant
- 16 for SOFCs, *J. Am. Ceram. Soc.* 97 (2014) 3835–3842.
- 17 <https://doi.org/10.1111/jace.13219>.
- 18
- 19 [23] M.K. Mahapatra, K. Lu, Glass-based seals for solid oxide fuel and electrolyzer
- 20 cells - A review, *Mater. Sci. Eng. R Reports*. 67 (2010) 65–85.
- 21 <https://doi.org/10.1016/j.mser.2009.12.002>.
- 22
- 23 [24] S.M. Gross, T. Koppitz, J. Rimmel, J.B. Bouche, U. Reisgen, Joining properties
- 24 of a composite glass-ceramic sealant, *Fuel Cells Bull.* 2006 (2006) 12–15.
- 25 [https://doi.org/10.1016/S1464-2859\(06\)71320-7](https://doi.org/10.1016/S1464-2859(06)71320-7).
- 26
- 27 [25] J. Schilm, A. Rost, M. Kusnezoff, S. Megel, A. Michaelis, Glass ceramics sealants
- 28 for SOFC interconnects based on a high chromium sinter alloy, *Int. J. Appl. Ceram.*
- 29 *Technol.* 15 (2018) 239–254. <https://doi.org/10.1111/ijac.12811>.
- 30
- 31 [26] H. Javed, A.G. Sabato, K. Herbrig, D. Ferrero, C. Walter, M. Salvo, F. Smeacetto,
- 32 Design and characterization of novel glass-ceramic sealants for solid oxide
- 33
- 34
- 35
- 36
- 37
- 38
- 39
- 40
- 41
- 42
- 43
- 44
- 45
- 46
- 47
- 48
- 49
- 50
- 51

- 1 electrolysis cell (SOEC) applications, *Int. J. Appl. Ceram. Technol.* 15 (2018) 999–  
2  
3  
4 1010. <https://doi.org/10.1111/ijac.12889>.
- 5  
6 [27] A.G. Sabato, A. Chrysanthou, M. Salvo, G. Cempura, F. Smeacetto, Interface  
7  
8 stability between bare, Mn–Co spinel coated AISI 441 stainless steel and a  
9  
10 diopside-based glass-ceramic sealant, *Int. J. Hydrogen Energy.* 43 (2018) 1824–  
11  
12 1834. <https://doi.org/10.1016/j.ijhydene.2017.11.150>.
- 13  
14  
15 [28] J. Schilm, A. Rost, M. Kusnezoff, A. Michaelis, Sealing Glasses for SOFC -  
16  
17 Degradation Behaviour, in: *Adv. Solid Oxide Fuel Cells V*, 2010: pp. 183–193.  
18  
19 <https://doi.org/10.1002/9780470584316.ch17>.
- 20  
21  
22 [29] D. Udomsilp, J. Rechberger, R. Neubauer, C. Bischof, F. Thaler, W. Schafbauer,  
23  
24 N.H. Menzler, L.G.J. de Haart, A. Nenning, A.K. Opitz, O. Guillon, M. Bram,  
25  
26 Metal-Supported Solid Oxide Fuel Cells with Exceptionally High Power Density  
27  
28 for Range Extender Systems, *Cell Reports Phys. Sci.* 1 (2020).  
29  
30 <https://doi.org/10.1016/j.xcrp.2020.100072>.
- 31  
32  
33 [30] A. Drewniak, D. Koszelow, P. Błaszczak, K. Górnicka, K. Jurak, H. Javed, A.G.  
34  
35 Sabato, P. Jasiński, S. Molin, F. Smeacetto, Glass-ceramic sealants and steel  
36  
37 interconnects: Accelerated interfacial stability and reactivity tests at high  
38  
39 temperature, *Mater. Des.* 212 (2021).  
40  
41 <https://doi.org/10.1016/j.matdes.2021.110259>.
- 42  
43  
44 [31] M. Ferraris, S. De la Pierre, A.G. Sabato, F. Smeacetto, H. Javed, C. Walter, J.  
45  
46 Malzbender, Torsional shear strength behavior of advanced glass-ceramic sealants  
47  
48 for SOFC/SOEC applications, *J. Eur. Ceram. Soc.* 40 (2020) 4067–4075.  
49  
50 <https://doi.org/10.1016/j.jeurceramsoc.2020.04.034>.
- 51  
[32] F. Smeacetto, A. Chrysanthou, A.G. Sabato, H. Javed, S.D. la Pierre, M. Salvo, M.

- 1 Ferraris, Glass-to-metal seals for solid oxide cells at the Politecnico di Torino, an  
2 overview, *Int. J. Appl. Ceram. Technol.* 19 (2022) 1017–1028.  
3  
4 <https://doi.org/10.1111/ijac.13949>.  
5  
6  
7  
8  
9 [33] B. Cela Greven, S. Gross-Barsnick, T. Koppitz, R. Conradt, F. Smeacetto, A.  
10 Ventrella, M. Ferraris, Torsional shear strength of novel glass-ceramic composite  
11 sealants for solid oxide fuel cell stacks, *Int. J. Appl. Ceram. Technol.* 15 (2018)  
12 286–295. <https://doi.org/10.1111/ijac.12819>.  
13  
14  
15  
16  
17  
18 [34] L. Wang, W. Yang, Z. Ma, J. Zhu, Y. Li, First-principles study of chromium di ff  
19 usion in the ferritic Fe-Cr alloy, *Comput. Mater. Sci.* 181 (2020) 109733.  
20  
21 <https://doi.org/10.1016/j.commatsci.2020.109733>.  
22  
23  
24  
25 [35] A.R. Kampf, R.C. Peterson, B.R. Joy, Itsiite,  $\text{Ba}_2\text{Ca}(\text{BSi}_2\text{O}_7)_2$ , a new mineral  
26 species from Yukon, Canada: Description and crystal structure, *Can. Mineral.* 52  
27 (2014) 401–407. <https://doi.org/10.3749/canmin.52.3.401>.  
28  
29  
30  
31  
32  
33  
34  
35  
36  
37  
38

### **Figure captions**

39 **Figure 1.** Configuration used for the mechanical tensile test.

40  
41 **Figure 2.** Heating Stage Microscopy (HSM) curves of the GC2 glass (5°C/min heating rate) on the  
42 Fe22Cr porous alloy (curve 1) and on the inert  $\text{Al}_2\text{O}_3$  support (curve 2); characteristic temperatures  
43 of GC2 glass identified with HSM are shown below the figure.  
44  
45  
46

47 **Figure 3.** Dilatometric curves of the GC2 as-cast glass (curve 1) and GC2 glass-ceramic obtained  
48 after sinter-crystallization at 950°C for 1h (curve 2); 5°C/min heating rate.  
49  
50

51 **Figure 4.** SEM images of the cross-section of (a) Crofer22APU/GC2 glass-ceramic/Fe22Cr porous  
alloy, (b) Crofer22APU/GC2 glass-ceramic interface (back-scattered) and (c) GC2 glass-  
ceramic/Fe22Cr porous alloy interface (back-scattered) obtained after sinter-crystallization at 950°C  
for 1h.

1 **Figure 5.** CT-scan of a Crofer22APU/GC2 glass-ceramic/Fe22Cr porous alloy joined sample  
2  
3 thermally treated at 950°C for 1 h. (a) 3D-model; sectioning plane (b) close to the porous alloy, (c)  
4 in the middle of the glass-ceramic, (d) close to Crofer22APU. The big pore on the right could  
5 probably be due to the manual slurry method used to produce the joined specimen.  
6  
7

8  
9 **Figure 6.** Cross-section FE-SEM images at lower (a) and higher (b) magnification of the Fe22Cr  
10 porous alloy/GC2 glass-ceramic interface after sinter-crystallization at 950°C for 1h; (c) infiltration  
11 of the glass-ceramic in the porous alloy of the joined sample; (d) EDS analyses of the GC2 glass-  
12 ceramic in the joining area.  
13  
14  
15  
16

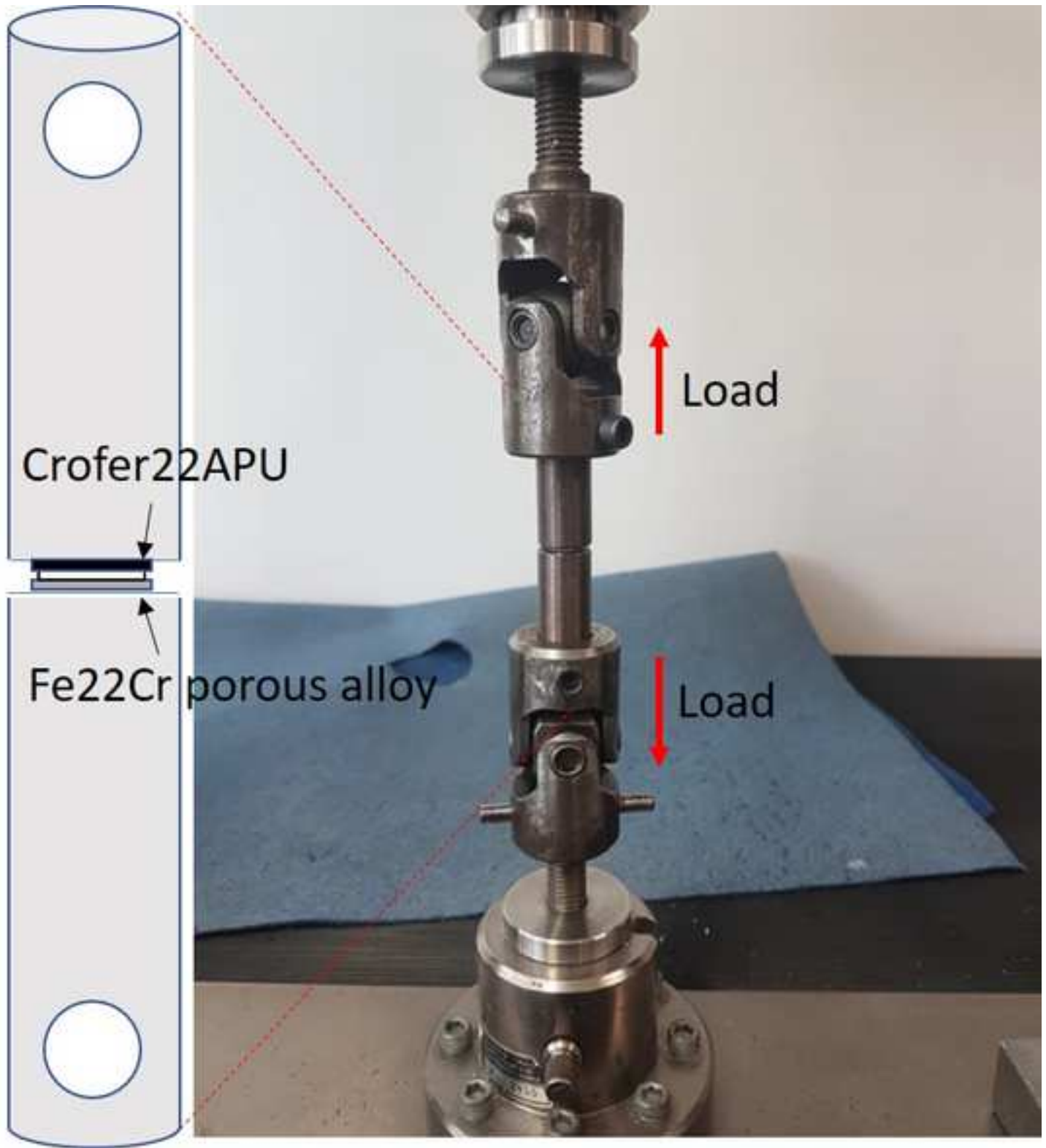
17 **Figure 7.** Macrographs of as-joined and aged Crofer22APU/GC2glass-ceramic/ Fe22Cr samples  
18 after tensile testing.  
19  
20

21 **Figure 8.** SEM images of top views of fracture surface of an as-joined (a) and an aged (b)  
22 Crofer22APU/GC2glass-ceramic/ Fe22Cr porous alloy sample after mechanical testing  
23 (Crofer22APU side); EDS analyses carried out on the fracture surfaces in the joining area.  
24  
25  
26

27 **Figure 9.** FE-SEM images of a cross-section after ageing at 700°C for 500hrs: (a,c) Fe22Cr porous  
28 alloy/GC2 glass-ceramic interface and (b) Fe22Cr porous alloy; (d) higher magnification of Fe22Cr  
29 porous alloy and EDS analysis carried out on the porosity edge of the porous alloy.  
30  
31  
32

33 **Figure 10.** XRD pattern of the fracture surface (Crofer22APU side) of a Fe22Cr/GC2 glass-  
34 ceramic/Crofer22APU joined sample after ageing at 700°C for 500 hrs.  
35  
36  
37  
38







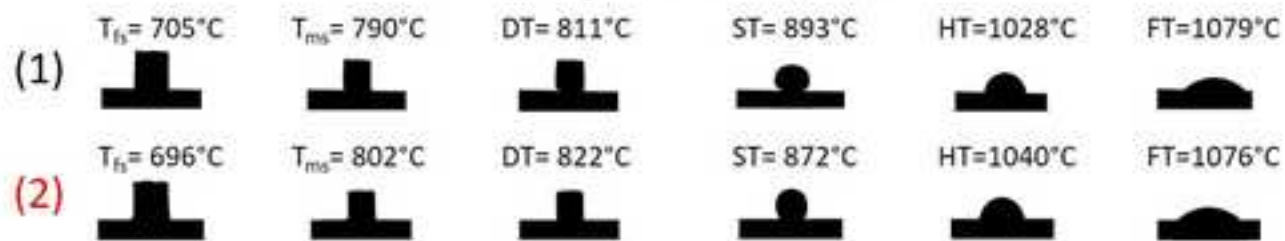
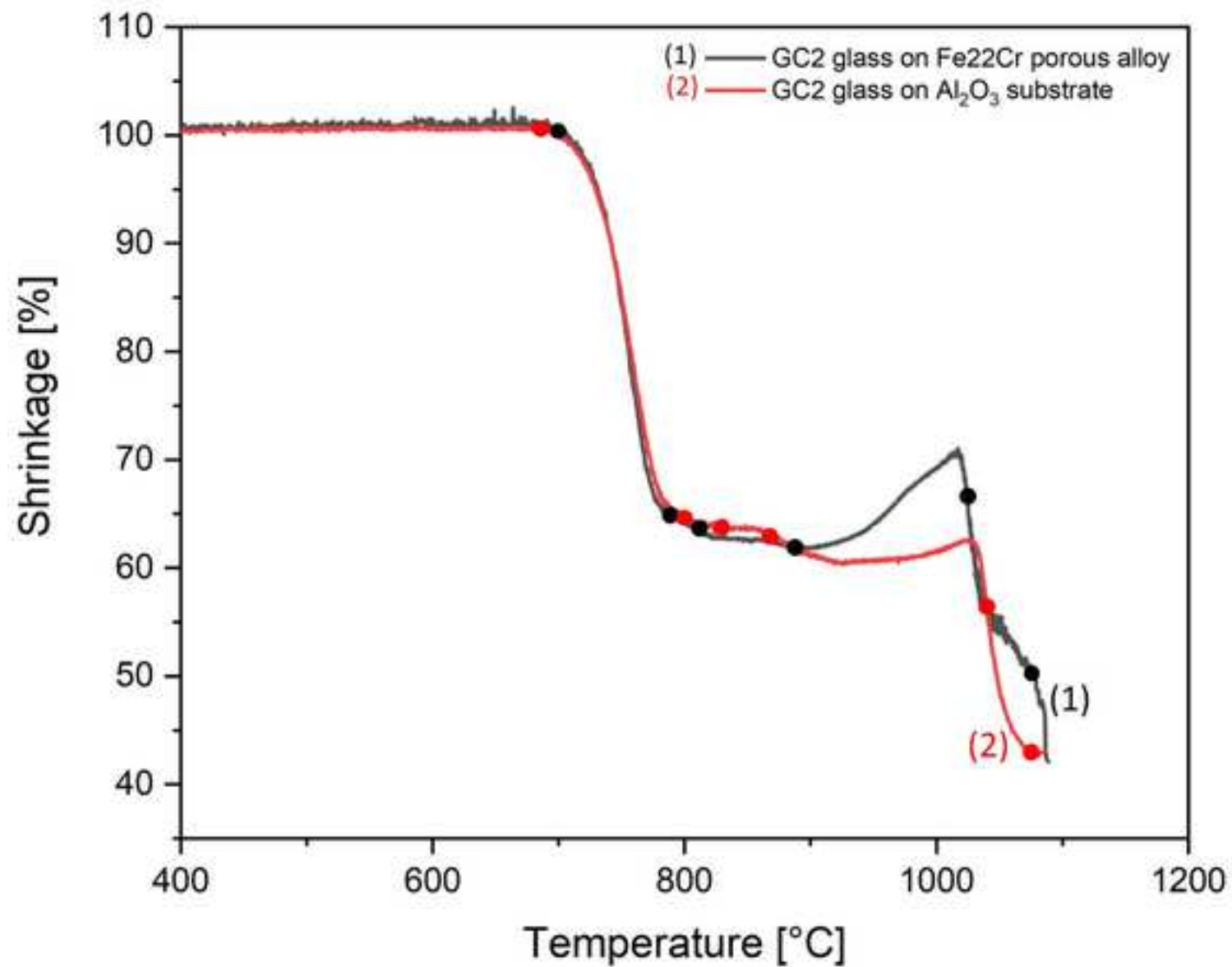
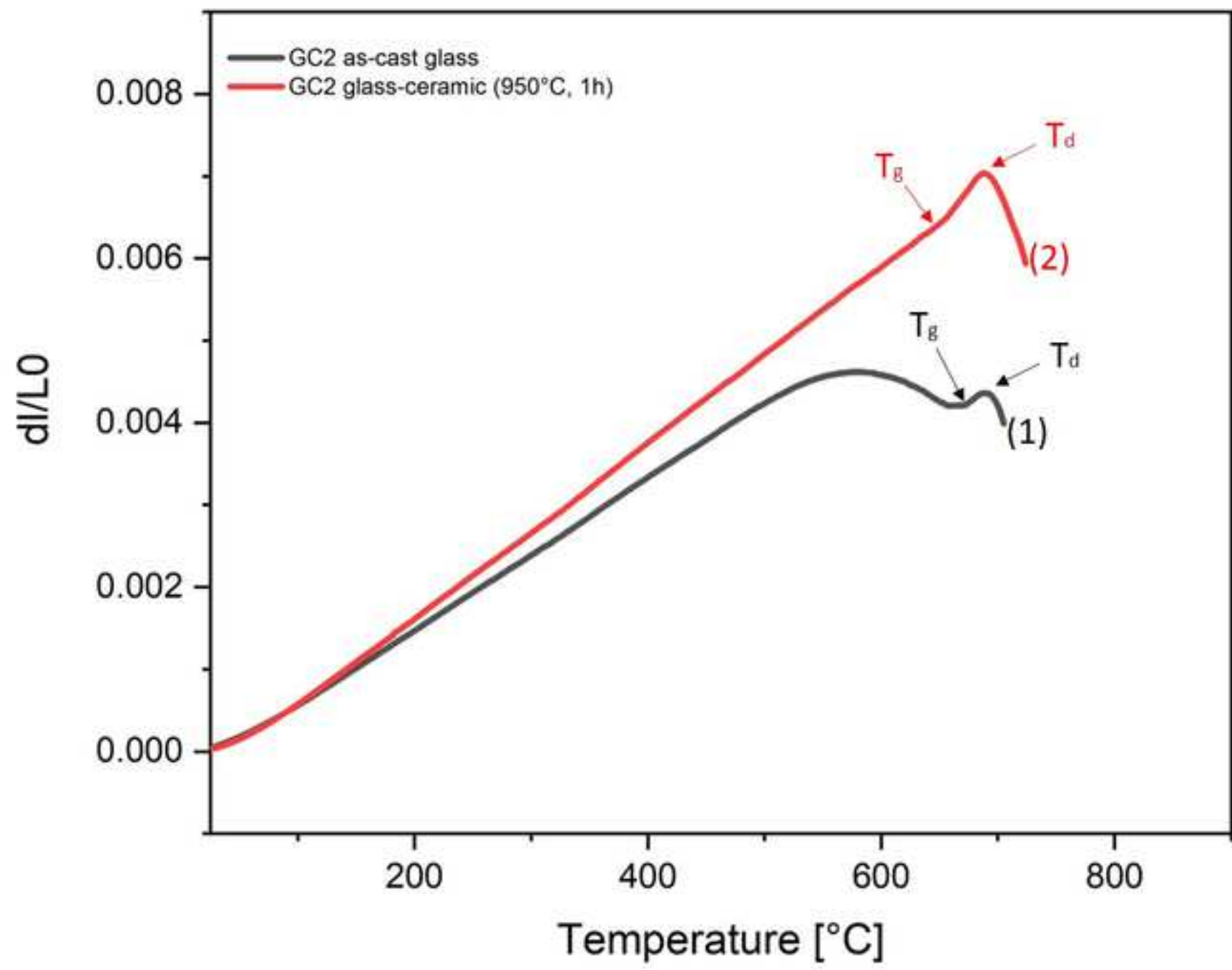
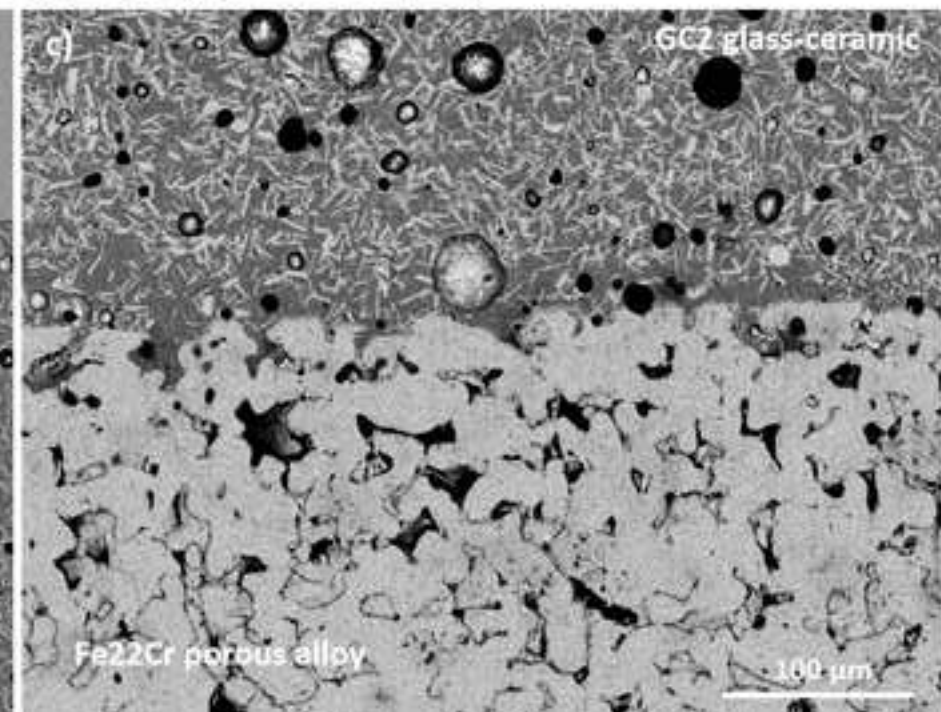
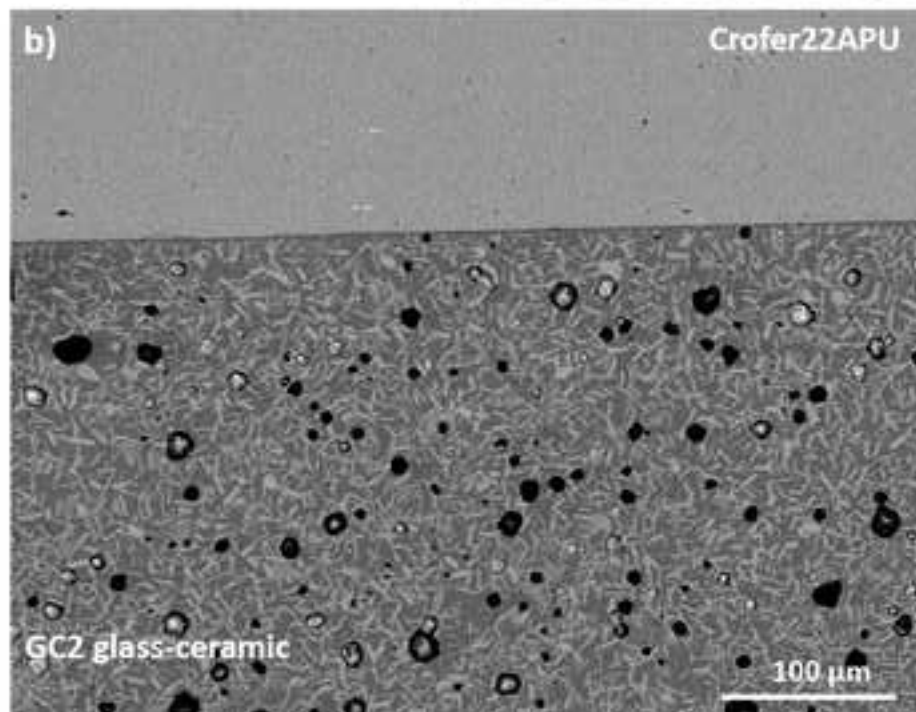
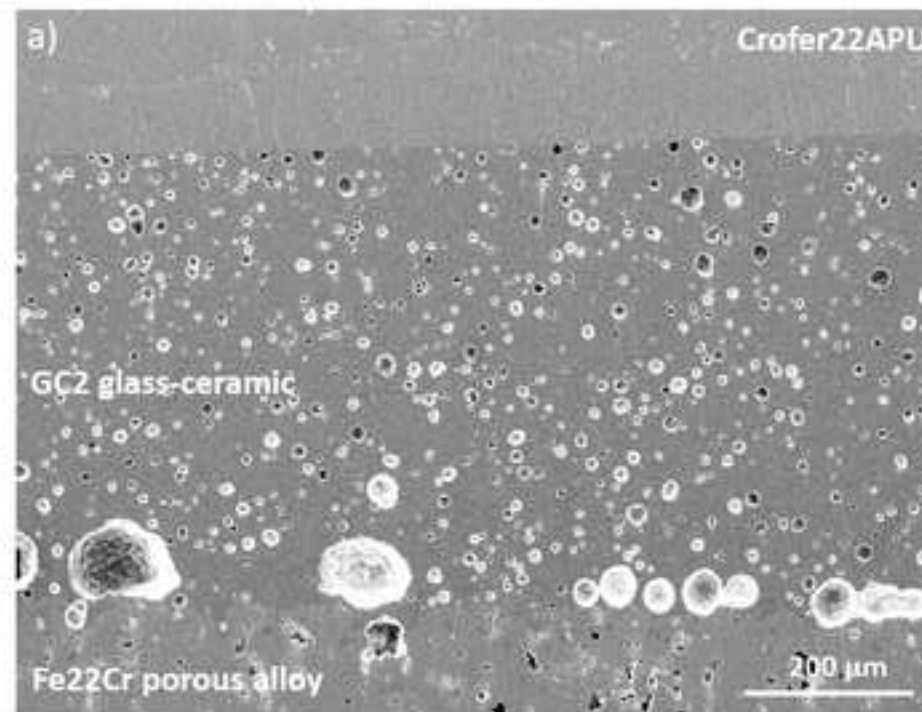
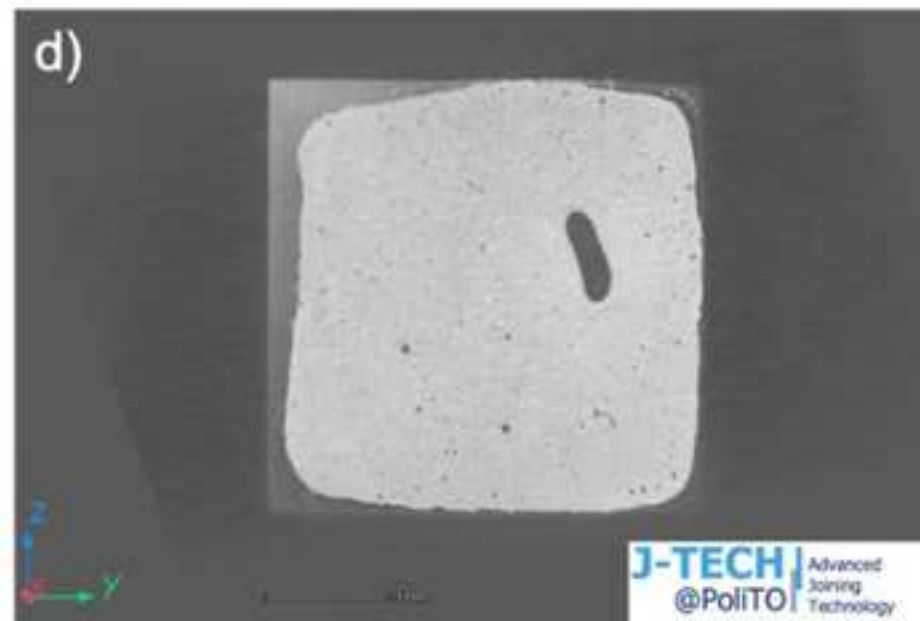
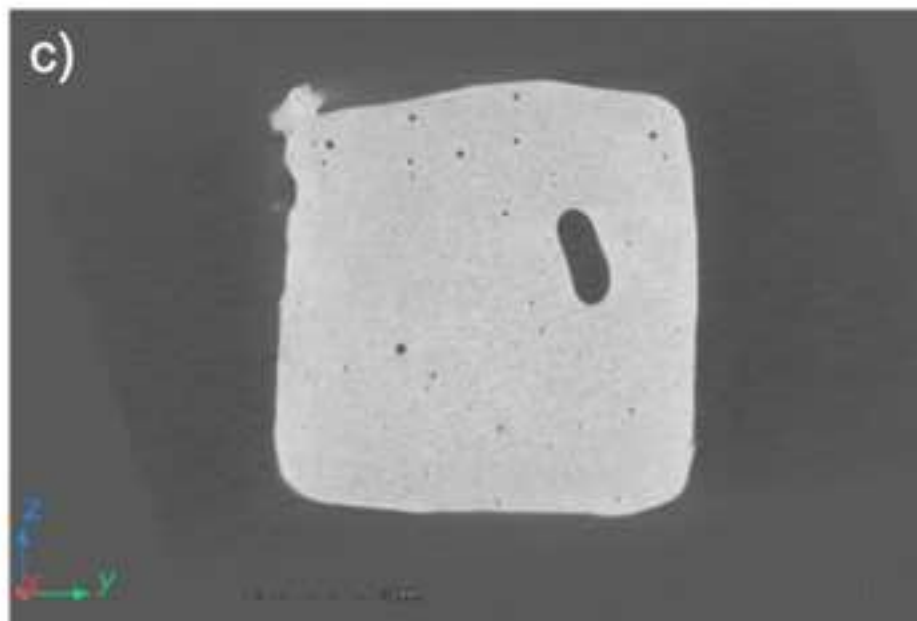
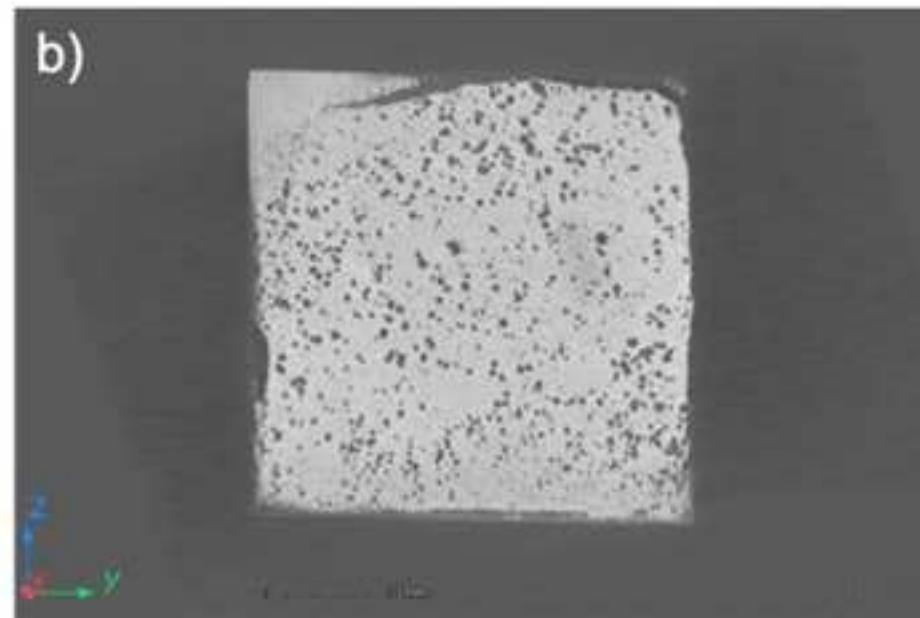
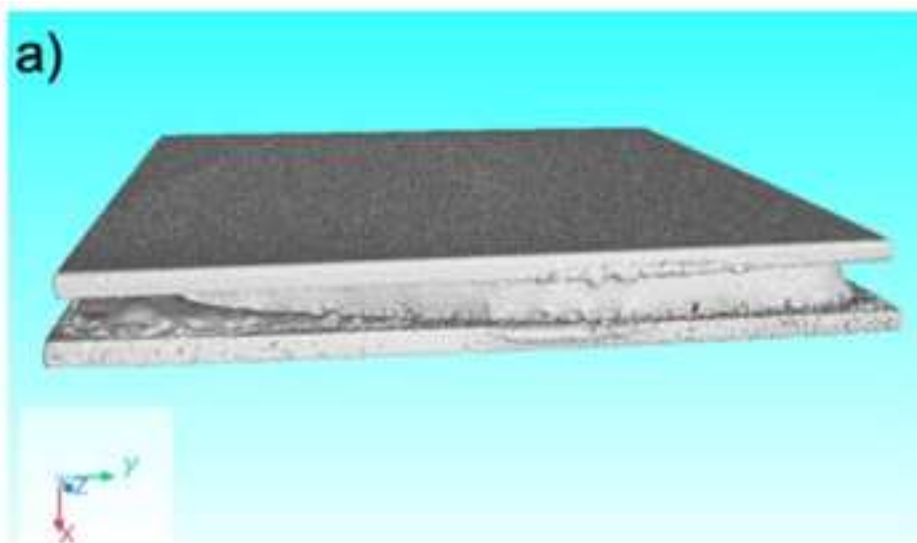


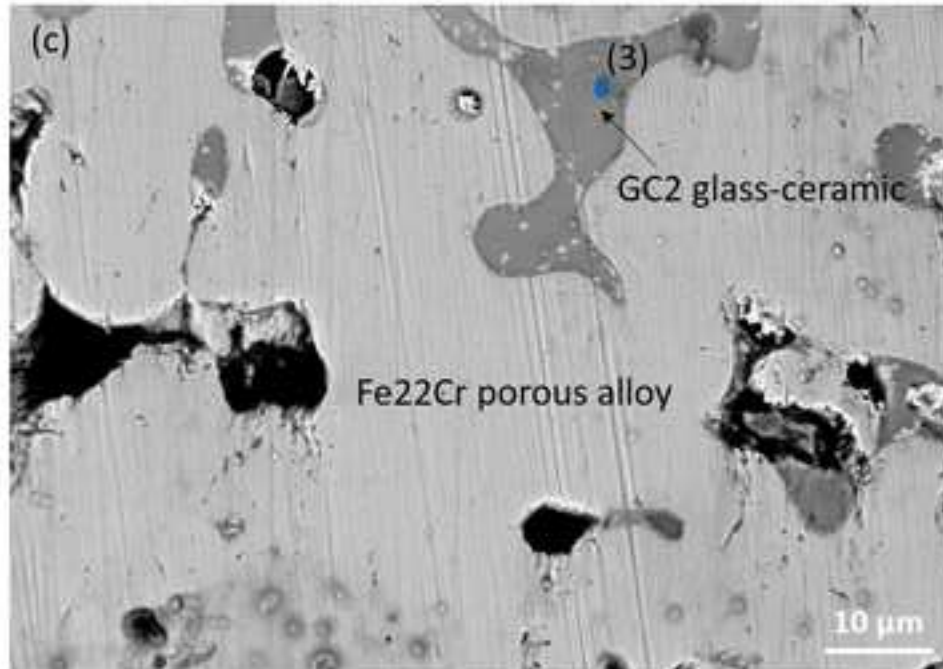
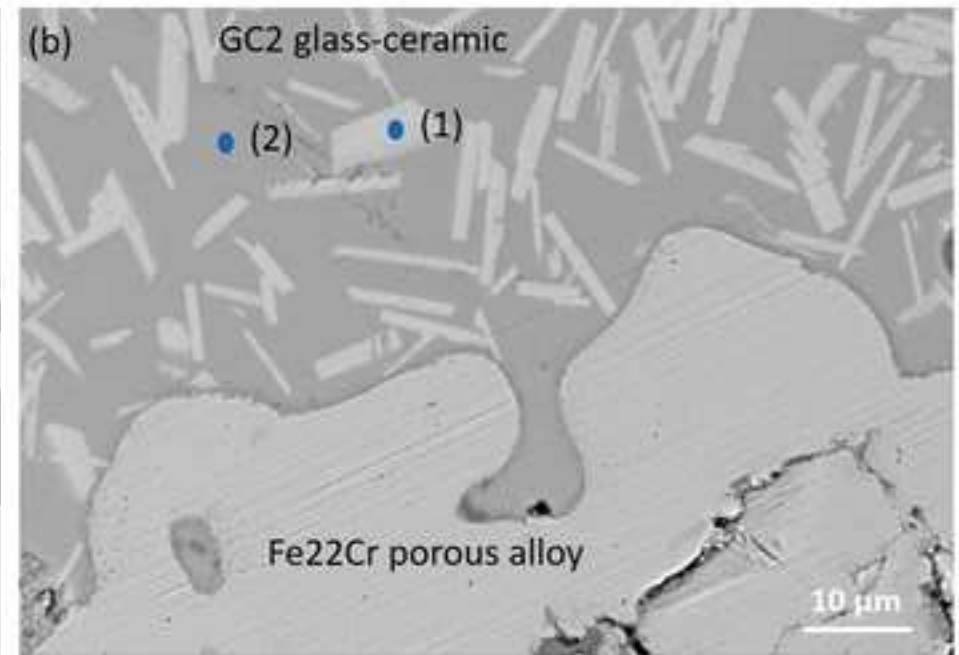
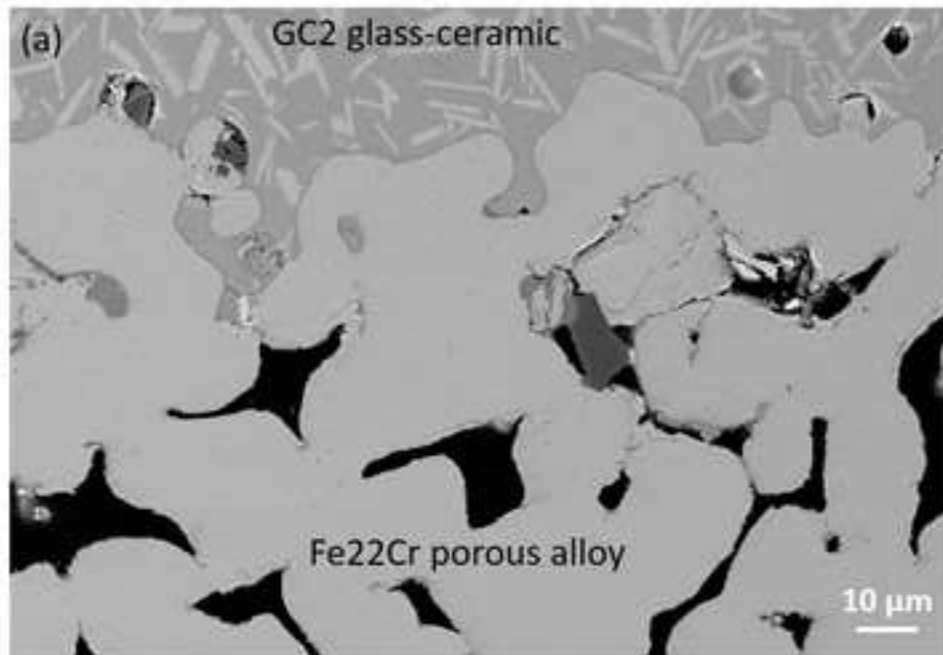
Figure 3








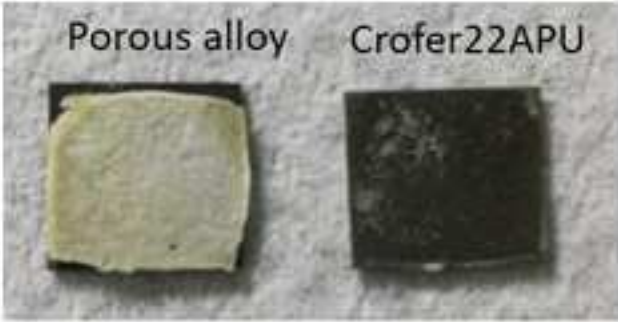
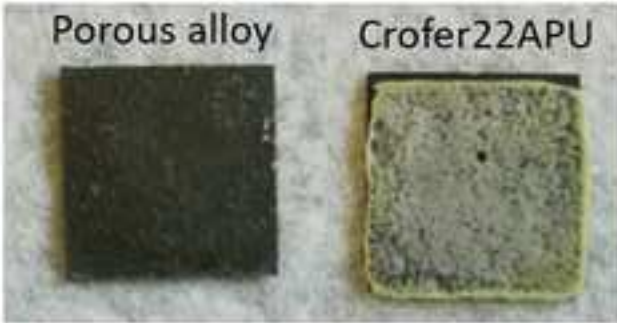







(d)

Elements	(1) Atomic %	(2) Atomic %	(3) Atomic %
O	61.7	65.1	63.7
Al	1.0	3.5	3.3
Si	25.1	20.5	22.2
Ca	1.2	2.9	2.7
Ba	11.2	8.0	7.1
Fe	-	-	1.0
Tot	100.0	100.0	100.0

Samples	Before ageing	After ageing
n.1		
n.2		
n.3		
$\sigma_m$ [MPa]	$7.4 \pm 0.5$	$7.7 \pm 2.9$

